Received 22 July 2021; | Revised 22 July 2021; | Accepted 22 July 2021

DOI: xxx/xxxx

Morphological changes of vanadyl pyrophosphate due to thermal excursions

Sepideh Badehbakhsh[1] | Nooshin Saadatkhah[1] | Mohammad Jaber Darabi Mahboub[2] | Olga Guerrero-Pérez[3] | Gregory S. Patience[1]

[1]Chemical Engineering, Polytechnique Montréal, C.P. 6079, Succ. "CV", Montréal, H3C 3A7 Québec, Canada

[2]Arkema Inc., 900 First Avenue, 19406 King of Prussia, PA, USA

[3]Departamento de Ingeniería Quimica, Universidad de Málaga, E-29071-Málaga, Spain

Correspondence

*Corresponding author Gregory S. Patience, Polytechnique Montréal Email: gregory-s.patience@polymtl.ca

Vanadyl pyrophosphate (VPP) is the active catalytic phase that converts n-butane to maleic anhydride in fixed beds, fluidized beds, and DuPont's circulating fluidized bed (CFB). The original CFB concept was based on the Mars van-Krevelen reaction mechanism in which the solid lattice contributes all of the oxygen to partially oxidize the n-butane. However, to achieve high reaction rates and selectivity requires the surface lattice to remain oxidized; thus, DuPont co-fed pure oxygen through 926 nozzles at three levels in the reactor. Since pure oxygen was fed independently of the butane stream, the gas composition at the nozzle crosses the explosion envelope and the local temperature could rise several 100 °C. Furthermore, the gas composition in the exhaust pipe downstream of the cyclone was within the explosion envelope. The temperature in these two locations periodically exceeded 700 °C, which was sufficiently high to deactivate the catalyst and turn it black. Here, we reproduced the high temperature conditions to examine the changes in catalyst morphology. A TA-Q500 heated the fresh catalyst to 800 °C under nitrogen and air flow. The VPP catalyst turned black above 700 °C in air but not in nitrogen. The catalytic surface area and pore volume of the fresh calcined catalyst decreased from 23 $m^2\ g^{-1}$ and 0.14 $cm^3\ g^{-1}$ to 12 $m^2\ g^{-1}$, and 0.09 $cm^3\ g^{-1}$ in the equilibrated catalyst. New bonds form and the active VPP reacts with silica to form $VO(P_2SiO_8)$.

1 | INTRODUCTION

With this article, we recognize the tremendous contributions of Gary L. Rempel to the field of catalysis. His first published work in Web of Science Core Collection was from 1973[1] and he had been extremely productive with a median of almost 6 articles per year over 46 years. Over 1/3 of his articles mention catalysis as a keyword and most of this work has been dedicated to polymerization (Figure 1). As many as 8 of his articles mention maleic anhydride, which he applied to functionalize and rubber[2] and grafting it to natural rubber[3,4]. This article focusses on morphological changes to a commercial vanadium pyrophosphate catalyst that DuPont developed to convert n-butane to maleic anhydride. The second step of the process converted maleic acid to THF, which was an intermediate to DuPont's Lycra® polyurethane block copolymer.

Vanadium and phosphorus are prominant elements of many industrial selective oxidation processes[6,7,8]. VPO compounds form crystalline phases for which the vanadium oxidation state varies from 5^+ (vanadyl phosphates γ, δ-$VOPO_4$), to 4^+ (vanadyl pyrophosphate $(VO)_2P_2O_7$), and 3^+ (vanadyl monophosphate VPO_4)[9,10,11]. The V-O-P phase and activity depend on vanadium oxidation state (5+, 4+, and 3+), the P to V ratio, the oxygen bond types at the edges, which dictate the catalytic performance,[6] and calcination/activation conditions. Oxygen coordinates at the surface to V or P as P=O and

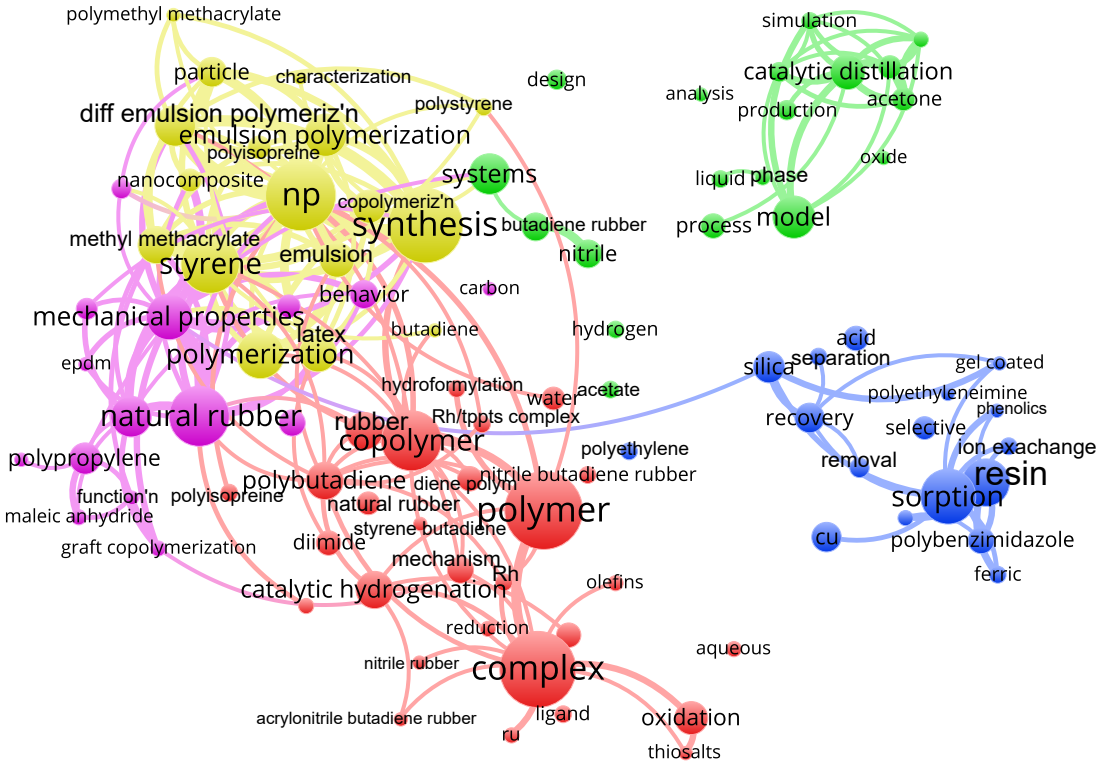

FIGURE 1 Keyword bibliometric map of the corpus of Gary Rempel's work from 1973 comprising 330 articles and 16 conference proceedings.[1,5]. The VOSViewer on-line program divides the 100 most common keywords into 5 clusters (same colour) where the size and font are proporotional to the number of articles that it appears: polymer (44 articles), model (22), sorption (31), synthesis(42), and natural rubber (34). The smallest circles for each category are thiosalts, (8), oxide (8) polyethyleneimene (8), polymethyl methacrylate (8), and functionalization(8). Lines represent citation links. Catalysis, with 120 occurences hydrogenation (79), and kinetics (66) were removed from the map because they dwarf the other themes so the circles would be too small to be noticeable.

V=O), double bridging (V–O–V, P–O–P, V–O–P), and triple bridging (V=O–P)[12,13].

The most selective phase is vanadyl pyrophosphate, $(VO)_2P_2O_7$ (VPP) that is produced from a topotactic transformation of the precursor—vanadyl hydrogen phosphate hemihydrate ($VOHPO_4 \cdot 0.5\,H_2O$)—at 390 °C in air[14]. Bulk vanadyl pyrophosphate creates an orthorhombic crystal layer with 16 V atoms and 16 P atoms with lattice parameters a=7.725 Å, b=16.576 Å, and c=9.573 Å[15,16]. A building unit contains two pairs of VO_6 octahedra joined together by PO_4 tetrahedra (Fig. 2)[6]. Adsorbates form bonds on the surface and penetrate into the lattice[6]. The electronic structure of the surface is the main reason for interaction and binding with the reactant(s). Several studies evaluated the electronic structure of the $(VO)_2P_2O_7$ surface, especially the behavior of differently coordinated surface oxygen sites at the surface of vanadyl pyrophosphate[6,17]. The activity of equilibrated catalysts varies with reaction conditions, phosphorous sublimation, which alters the catalyst P/V ratio, changing vanadium oxidation state, sintering, loss of surface area (due to localized hot spots), and poisons (sulphur accompanying the butane feed, for example)[18].

Vanadyl pyrophosphate catalyzes various classes of reaction with high selectivity (Table 1). Different steps have been proposed to characterize the mechanism to produce maleic anhydride from n-butane[19]. Chemistries include oxyfunctionalization of light paraffins such as oxidation of ethane to acetic acid, propane oxidation to acrylic acid, propane ammoxidation to acrylonitrile, and n-butane and n-pentane partial oxidation to maleic and phthalic anhydrides[13,20,21,22,23,24]. It selectively dehydrates glycerol to acrolein due to its mild acid-basic properties but is less active in the one-step process to acrylic acid.[25]. Molecular oxygen reduces coke formation and minimizes side reactions[25]. Industrially synthesized and shaped vanadium phosphate performed poorly in the ammoxidation of 3-picoline due the solid-state transformation of the hemihydrate precursor into an ammonium-containing VPO

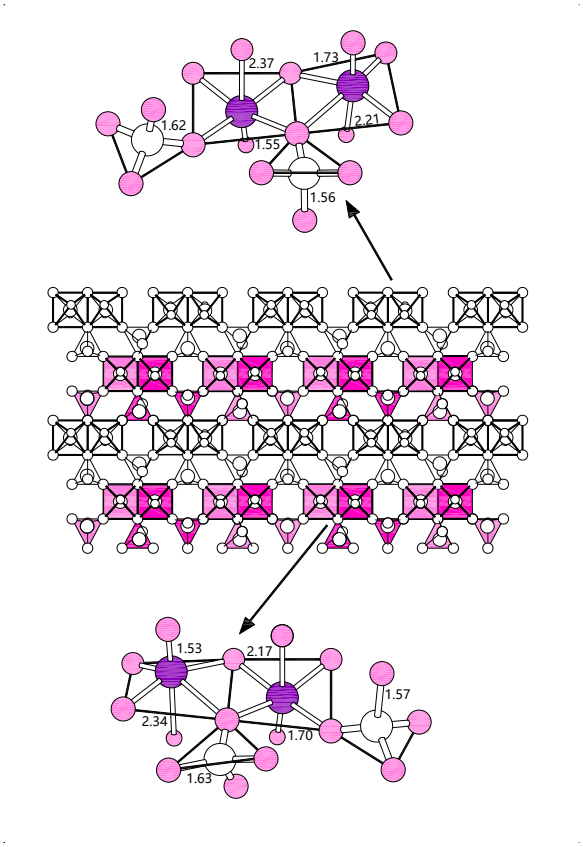

FIGURE 2 The $(VO)_2P_2O_7$ (100) structure. The dark and light gray circles refer to V and O atoms,respectively, while P centers are white. All distances in the figure are in Å [6].

phase. The calcined vanadyl pyrophosphate yielded nicotinonitrile up to 80 % as the selectivity approached 100 %. The equilibrated catalyst sample had poorer catalytic performance due to the reduced vanadium species and carbonaceous surface depositions [26]. $(VO)_2P_2O_7$ ammoxidizes propane to acrylonitrile and has been tested [21,8] to produce furan from butadiene [27].

The partial oxidation of n-butane to maleic anhydride remains the largest application of VPP [6,7,8] in both fluidized bed and fixed bed reactors [28,29]. The catalyst abstracts eight atoms of hydrogen and inserts three oxygen atoms. This multi-step reaction mechanism occurs entirely on the adsorbed phase [28]. Fixed bed hot spot temperatures exceed 450 °C. DuPont commercialized circulating fluidized bed technology (CFB) that operated at 400 °C and 3 bar gauge at the exit (Figure 3) [30,31]. The maximum operating temperature was constrained by the carbon steel vessel. In this technology, the catalyst entered the base of the fast bed and was transported upwards to the riser at 6 m s^{-1}. The diameter and height of the riser were 1.8 m and 25 m, while the fast bed with a diameter of 4.2 m was 11 m tall and had two sets of cooling coils and three

TABLE 1 Classes of reactions catalyzed by vanadyl pyrophosphate [19].

Reaction type	Reactant	Product
Oxydehydrogenation	Isobutyric acid	Methacrylic acid
	Cyclohexane	Benzene
	Succinic anhydride	Maleic anhydride
	Hexahydrophthalic anhydride	Phthalic anhydride
	Paraffin	Olefin
Allylic oxidation: H-abstraction or O-insertion	Olefin	Diolefin
	2,5-Dihydrofuran	Furan
	Tetrahydrophthalic anhydride	Phthalic anhydride
Electrophilic oxygen-insertion	Benzene	Maleic anhydride
	Naphthalene	Naphthoquinone
	Furan	Maleic anhydride

oxygen spargers with 926 nozzles per sparger (Fig. 3) [32]. The (CFB) transferred the catalyst from a net oxidizing zone to a net reducing zone [30,33]. In the air fed regenerator, a fraction of the surface vanadyl pyrophosphate species oxidized from the V^{4+} state to the V^{5+} state while in the fast bed, the n-butane reduced the V^{5+} species to V^{4+}.

The surface of VPP has strong Bronsted sites as well as medium strong and very strong Lewis sites in different ratios [35,36,37]. The vanadium oxidation state (acid sites) in the reaction condition controls the selectivity and activity of the catalyst [19] since the C-H bond cleavage on n-butane interacts with both a Lewis acid site (V^{4+}) and a Brønsted acid site (P-OH) on the surface of vanadyl pyrophosphate [8,38,39,40]. The Lewis/Brønsted ratio decreases with temperature [41]. The nature of V-P-O phases formed during the thermal treatment and at operating conditions determines the average vanadium oxidation state [42,43].

Here, we characterized precursor, fresh, and equilibrated VPP to identify phase changes, catalyst structure deformation, and catalyst deactivation formulation and phases due to thermal excursions that occured at DuPont's CFB facility in Asturias, Spain. The equilibrated-catalyst, calcined VPP, and precursor were provided by DuPont. [44]

2 | MATERIALS AND METHODS

The two methods to produce VPP include:

1. An aqueous HCl method followed by a water extraction step;
2. Reaction of V_2O_5 with H_3PO_4 in isobutanol and benzyl alcohol [45].

Patience at al. [14] synthesized VPP precursor on a commercial scale in an organic medium with isobutanol and benzyl

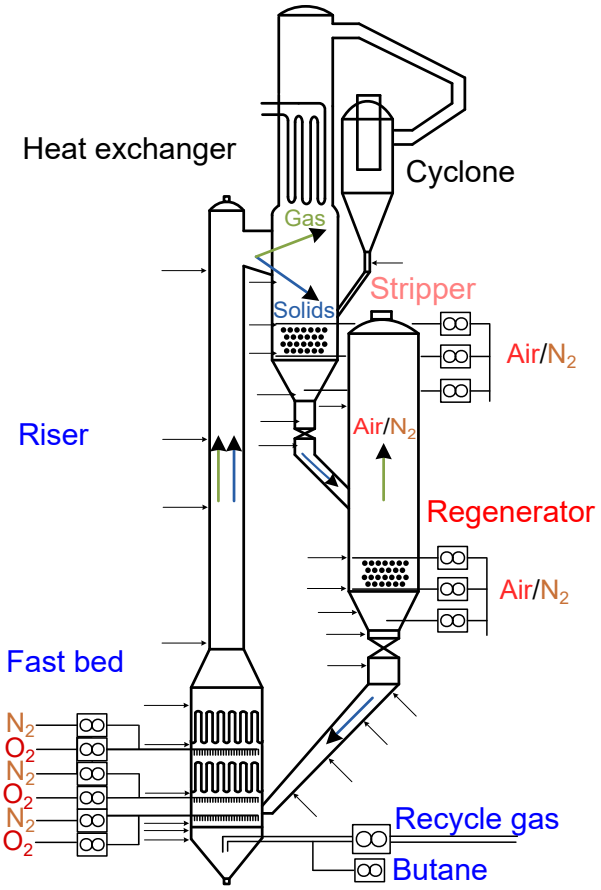

FIGURE 3 DuPont's commercial circulating fluidized bed configuration. A third oxygen sparger was added below the solids side entrance in the fast bed to maintain the catalyst at a higher oxidation state rather than allowing the butane/recycle gas to reduce the catalyst before reoxidation. The arrows represent pressure taps to measure catalyst inventory. The heat exchanger at the top of the stripper was added to reduce off gas burning that turned fine particles black. Air, nitrogen, recycle gas, and enriched air were possible gases to strip interstitial gas of n-butane and maleic anhydride. Steam failed as a stripping gas as VPP agglomerates easily, even at 400 °C. Enriched air was fed to the regenerator to accelerate the reoxidation process. Reproduced from Patience[34]. Copyright Elsevier 2017.

alcohol. The precursor was micronized to 2.5 µm, then spray-dried with polysilicic acid to form a porous silica shell. The median particle diamter was 70 µm and the porous shell was on the order of 10 µm. Amoro's et al.[46] synthesized a series of vanadyl hydrogenphosphate hydrates (α-, β-$VOHPO_4.2H_2O$, $VOHPO_4.3H_2O$, $VOHPO_4.4H_2O$)(Fig. 4)[7]. We characterized the morphological changes between precursor, calcined catalyst, equilibrated catalyst, and black powder generated in the laboratory. We measured physical properties like the particle size distribution, surface area, minimum fluidization velocity (Table 2) and chemical properties with XRD, XPS, Raman, and EDS.

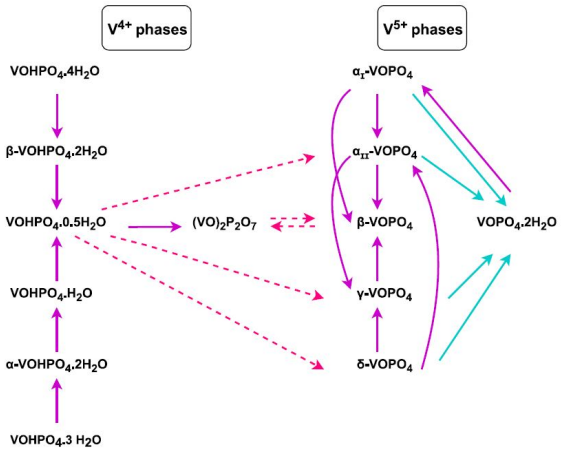

FIGURE 4 Diagram of phase transformations of VPO catalysts and precursors[7].

TABLE 2 Powder properties.

Property	Prec.	Calc.	Eq.	n	Comment
U_{mf}, mm s^{-1}	9.4	4.1	3.8	3	D_t = 8 mm
	905	898	1098	5	Scott density
ρ_b, kg m^{-3}	913	913	1114	5	poured density
	997	1033	1259	5	tapped density
	1551	2089	2018	5	particle density
ρ_p, kg m^{-3}		1915	2757	1	MIP
ρ_p, kg m^{-3}		1713	1959	1	MIP
ρ_{sk}, kg m^{-3}	2496	2739	2774	10	gas pycn.
A, m^2 g^{-1}		10.7	0.08	1	MIP
θ, °	26	24	23	6	angle of repose
d_p, µm	88	67	59	3	Mean size
d_p, µm	79	59	55	3	Median size
s_A, m^2 g^{-1}	22	23	12	1	BET
	34	28	15	1	BJH
v_{pore}, mL g^{-1}	0.11	0.14	0.09	1	BET
R_{pore}, Å	19.12	19.06	19.08	1	BET, BJH
O, g g^{-1}	0.50	0.50	0.43	5	EDX
V, g g^{-1}	0.24	0.22	0.27	5	EDX
P, g g^{-1}	0.18	0.17	0.21	5	EDX
Si, g g^{-1}	0.09	0.11	0.07	5	EDX
Fe, g g^{-1}	0	0	0.03	5	EDX
V, g g^{-1}		0.42	0.41	6	XRF
P, g g^{-1}		0.09	0.08	6	XRF
Si, g g^{-1}		0.03	0.02	6	XRF
Fe, g g^{-1}		0.0	0.01	6	XRF

An Empyrean Panalytical diffractometer recorded X-ray diffraction (XRD) patterns at ambient temperature by Cu K$\alpha_{1,2}$ (1.5406 Å) monochromatic radiation at 45 kV and 40 mA. It scanned the diffraction angle between 5° to 80° for 30 min with a PIXcel detector and Soller slits (incident and diffracted beam) of 0.04 rad (Figure 11).

An LA-950 Horiba laser diffraction analyzer measured the particle size distribution (PSD) based on the Mie theory (Table 2)[47]. An AUTOSORB-1 (Quantachrome Instruments, USA) measured the surface area of the powder samples by the standard multi-point Brunauer–Emmett–Teller (BET). The samples were degassed at 200 °C to evaporate residual water overnight. We applied the Barret–Joyner–Halender (BJH) method to determine the pore size distribution. A Quantachrome Poremaster PM 3312 mercury porosimeter measured pore volumes by intrusion and extrusion curves, over a dried degassed sample, up to 228 MPa. It covered a pore diameter range from 0.0070 µm to 1000 µm[48]. A Thermogravimetric Analyzer (TGA Q500) measured the mass change rate of the samples as a function of both temperature and time in a controlled atmosphere with a resolution of 0.1 µg and an accuracy of 0.1 %. The maximum load for the TGA Q500 is around 0.1 g, but loading more than 20 mg, decreases the mass transfer rate due to the shielding of sample on the pan[49,50]. We measured volume and density of the samples with an AccuPyc 1340 Folio Instrument with three different chamber volumes (1, 3.5 and 10 mL) (Table 2).

An Invia Reflex Raman Confocal (RENISHAW) spectrometer equipped with a a RemCam deep depletion CCD detector of 514.5 nm Ar line, and a spectral resolution of ca. 1 cm^{-1} acquired the Raman spectra of the samples in the 200 cm^{-1} to 3200 cm^{-1} region. We treated the samples in a mixture of 21 % oxygen in argon at various temperatures in a Linkan in-situ cell to record the spectra[51]. An epsilon 4 benchtop EDXRF spectrometer quantified silicon, phosphorus, vanadium and iron in the samples. This spectrometer had a silver anode x-ray tube, 50 kV excitation capabilities, a maximum current of 2 mA and a maximum power of 10 W, to analyze elements non-destructively.

A 5700C Physical Electronics X-ray photoelectron spectroscopy (XPS) apparatus analysed the surface chemistry of the samples with MgKα radiation of 1253.6 eV. We shifted all the peaks with a reference to the maximum of the C1s peak at 284.5 eV[52]. A field emission scanning electron microscope (FE-SEM-JEOL JSM-7600F) captured images at a voltage of 5 kV and an energy range of 10 keV. Scanning electron microscopy energy dispersive X-ray spectroscopy (SEM-EDS) recorded P, V, and Si distribution in the powders. To observe cross section of the particle, we mounted them on Technotherm® 3000 and polished it with monocrystalline diamond suspension.

3 | RESULTS AND DISCUSSION

The catalyst changed color during the synthesis process and in the CFB reactor. The precursor was olive green and turned a deeper green after calcination (Figure 5). Most of the calcined VPP was green but there were an occasional black particle (< 1 %). Equilibrated catalyst particles were mostly brown and black: as much as 50 % of the particles smaller than 45 µm were black while less than 20 % of the particles greater than 90 µm were black (Figure 6). Independent tests in bench scale reactors were capable of turning the VPP particles to black above 700 °C.

In the first day of operation during the commisioning the commercial plant, as much as 10 % of all the catalyst turned black due to back flow of n-butane up the regenerator standpipe. The temperature in this region was sufficiently high to deform the stainless-steel slide valve that controlled the solids circulation rate (< 700 °C). An infrared gun reported an outside skin temperature on the metal standpipe greater than 500 °C during this event that lasted 9 h. To minimize n-butane backflow into the standpipe, the commercial team redirected the solids flow upward by about 30° with an insert. This was the first in a series of modifications to improve the plant operability. The second area that caused black solids was the exhaust pipe in the region of the cyclone. VPP powder effectively quenches free radicals thus minimizing thermal excursions. However, downstream of the cyclone, the solids hold-up is insufficient to quench n-butane free radicals and so the oxygen (< 4 %) would react with they hydrocarbon and the fine particles present would turn black. Most of these fine particles returned to the regenerator but particles less than 20 µm were carried to sintered metal filters. This problem was solved by installing a heat exchanger immediately above the stripper to drop the temperature by over 100 °C.

Both VPP color and activity activity remained constant in lab-scale reactors. In the pilot plant and commercial reactor, activity dropped and surface area as the fraction of black powder increased. Coincidentally with the drop of activity, the catalyst surface area decreased[30,31].

Over 100 thermcouples were positioned throughout in the fastbed at the sparger nozzle tips, in the standpipe, in the cyclones, and the exhaust piping but none recorded temperatures near 700 °C. Sudden changes in the local temperature in the fast bed were as much as 40 °C, but more often the dozens of thermcouples positioned at the nozzles tips recorded temperature rises on the order of 2 °C[31,32]. In the pilot plant demonstration, catalyst also turned black due to thermal excursion at the sparger tips. Thermcouples positioned at the tips recorded instantaneous temperature rises of 1 °C to 10 °C and these were accompanied by a simultaneous drop in oxygen concentration and an increase in carbon dioxide (often < 1 %).

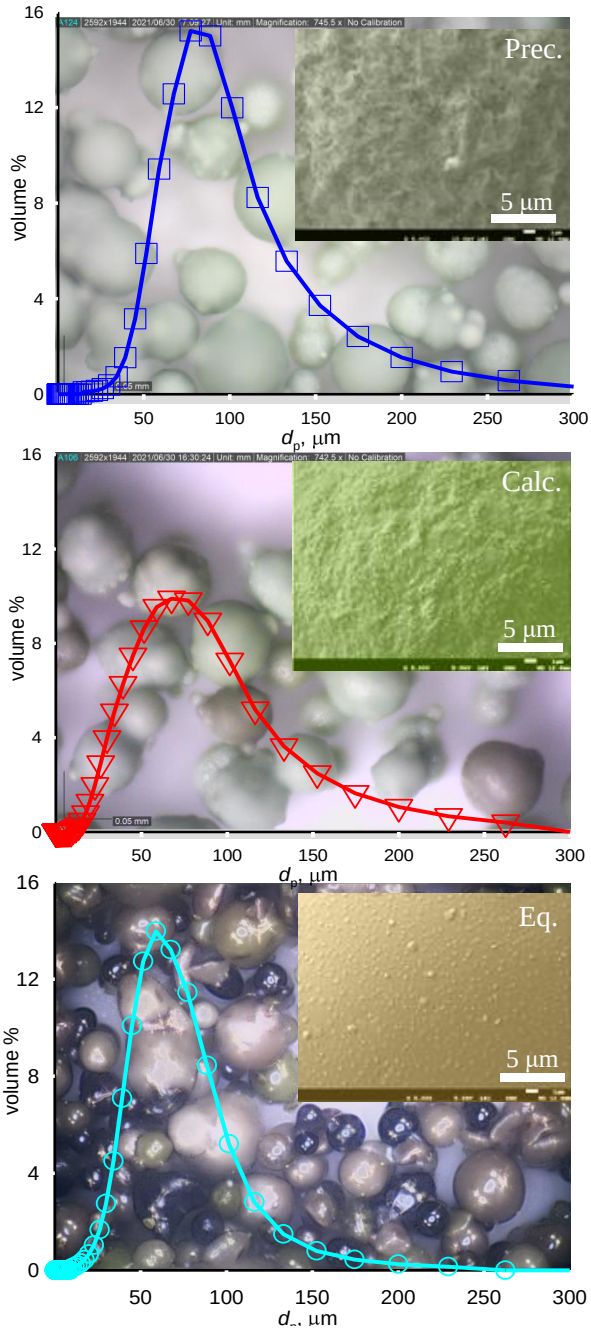

FIGURE 5 Microscope images and particle size distribution of precursor at the top (Prec.), calcined VPP in the middle (Calc.), and (c) equilibrated catalyst at the bottom (Eq.). The insert at the top left of each panel are SEM images of the surface. The colour of the surface were matched to correspond to the colours of the powder in daylight.

The mean particle size of the precursor was highest at 88 µm, followed by the calcined VPP at 67 µm, and 59 µm for the equilbrated catalyst (Table 2). The calcined VPP had the broadest particle size distribution. Both the precursor and calcined VPP have satellite particles attached to the exterior surface that cleaved in the reactor as the catalyst circulated in the loop at over 4 kt h^{-1}. The images of the equilbrated VPP are very shiny: the white outline of each particle is reflected light from the lamp illuminating the surface. Both the precursor and calcined catalyst have a matt texture and so the reflected light is more dispersed.

The minimum fluidization velocity (U_{mf}) of VPP calcined and equilibrated-catalyst are 4.1 mm s^{-1} and 3.8 mm s^{-1}. VPO precursor has the highest U_{mf} among the three samples at 9.4 mm s^{-1}. Samples of the black powder had a lower surface area compared to either the calcined VPP or equilibrated catalyst, which implies that structure has collapsed somewhat.

3.1 | Physical characterizations

SEM-EDX detected vanadium, oxygen, phosphorus and silicon in all three catalysts (Table 2). The weight percent of both oxygen and silicon dropped during partial oxidation of n-butane to maleic anhydride, while the weight percent of vanadium and phosphorus increased moderately. Only the equilibrated-catalyst contains Fe.

Precursor, calcined and equilibrated samples all have a shell of silica (Figure 7 and Figure 8) covering a porous structure. Some particles have hollows cores with holes up to 20 µm.[53]

VPP is a micro-mesoporous material with pore diameter of 19 Å[54]. Calcined VPP and the precursor have higher BET and BJH surface area and pore volume compared to the equilibrated catalyst (Table 2). Both surface area and pore volume of VPP decreased from 23 m^2 g^{-1} and 0.14 cm^3 g^{-1} to 12 m^2 g^{-1} and 0.09 cm^3 g^{-1} in equilibrated-catalyst. The desorption path differs from the adsorption path, creating a hysteresis loop type H3 (Figure 9). The loops of type H3 typically exists in solids consisting of aggregated non-rigid plate-like particles[55].

The total surface area of VPP calcined is much higher than that of the equilibrated-catalyst, while both particle density and the bulk volume of the equilibrated-catalyst are higher compared to calcined VPP (Table 2). This suggests that during partial oxidation of n-butane to maleic anhydride, the total surface area decrease significantly, while the particle density increase slightly due to a loss of porosity.

3.2 | Chemical characterizations

We heated all three samples in both nitrogen and air at a heating rate of 10 °C min^{-1} until 800 °C followed by an isothermal hold of 30 min in TGA (Figure 10). Up to 400 °C, all samples change mass in both air and nitrogen in a similar manner (loss of water). Above 400 °C in air, all the catalysts begin to gain 2 % mass, but in nitrogen, they continue to lose mass. All the samples turned black in air, but not in nitrogen.

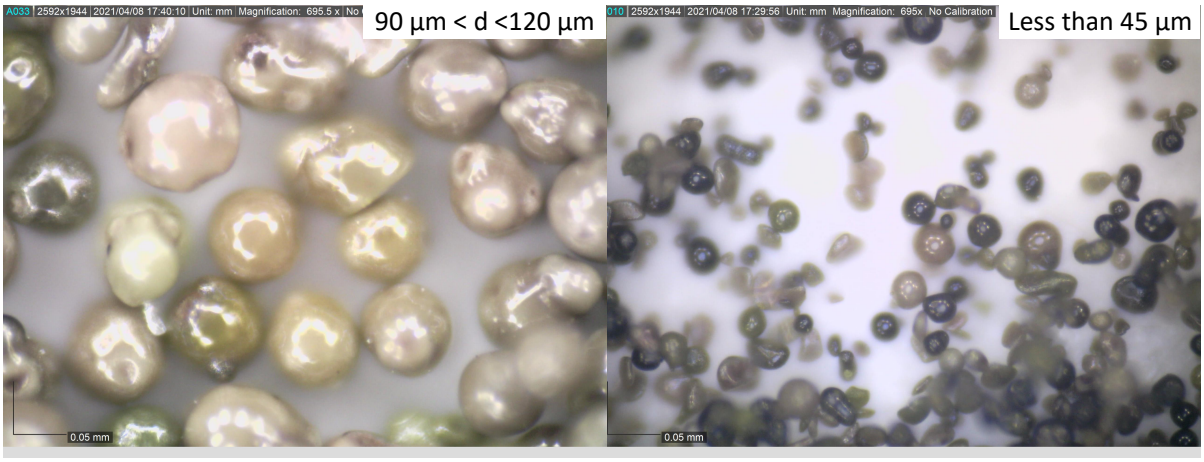

FIGURE 6 Microscope images of equilibrated catalyst: 90 µm < d_p < 120 µm (left panel), d_p <45 µm (right panel). Black particles are more prevelant in the sample with the smallest particle diameter.

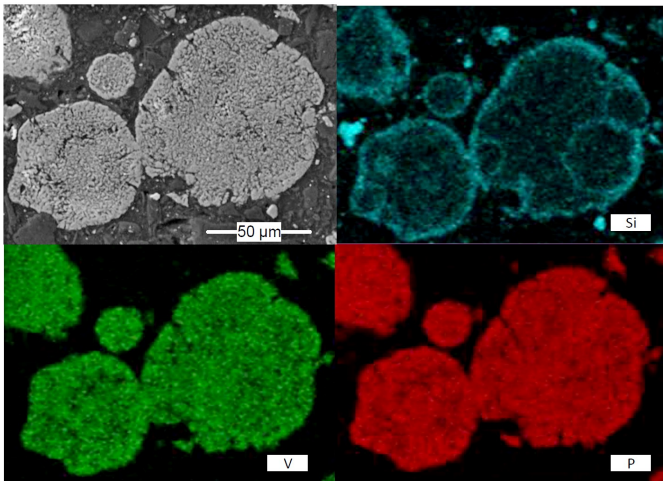

FIGURE 7 EDS elemental mapping of the calcined catalyst. The silica forms a 10 µm shell around the VPP in the centre. The original mechanism proposed by DuPont to account for the thicker shell assumed that Si migrated to the surface from the interior. However, since the interior of the catalyst microsphere still has Si, the most likely scenario is that during the spray drying process, as water evaporates, the particle shrinks and the Si in the liquid remains at the surface and polymerizes.

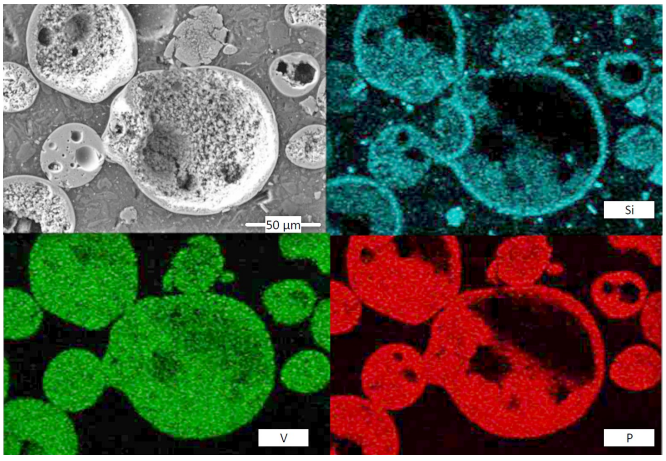

FIGURE 8 EDS elemental mapping of the equilibrated catalyst. The silica shell appears to be somewhat more dense in this sample compared to the calcined VPP.

In air, with increasing temperature up to 400 °C to 600 °C, the mass dropped for all three samples, then slightly increased reaching a maximum at around 700 °C and then the mass dropped again until it stabilized at 800 °C (98.3 %, 92.5 %, and 87 % for equilibrated-catalyst, calcined VPP, and precursor, respectively).

We associate the first mass loss to evaporation of physisorbed and chemisorbed water. The increase in mass around 700 °C happened only in air, which is due to the oxidation of vanadium or phosphorous since oxygen was the only available reactant. The slight weight loss after 700 °C is associated with degradation of vanadium and phosphorous oxides and a decrease in their oxidation states that forms other oxides like VO_2, $VO_{0.2}$, $VO_{1.27}$.

The main phases detected by XRD in calcined VPP are $(VO)_2P_2O_7$ and $VO(HPO_4) \cdot 0.5\,H_2O$; in VPP equilibrated are $(VO)_2P_2O_7$; and in precursor they are $VO(HPO_4) \cdot 0.5\,H_2O$ (Figure 11). Up to 250 °C in nitrogen, the mass of the equilibrated-catalyst, VPP calcined and VPO precursor decreased 3.7 %, 12.5 % and 18 % of the original mass due to the elimination of H_2O and formation of $(VO)_2P_2O_7$ [56]. Precursor and calcined VPP lose both physisorbed and chemisorbed water (Figure 10), while equilibrated-catalyst

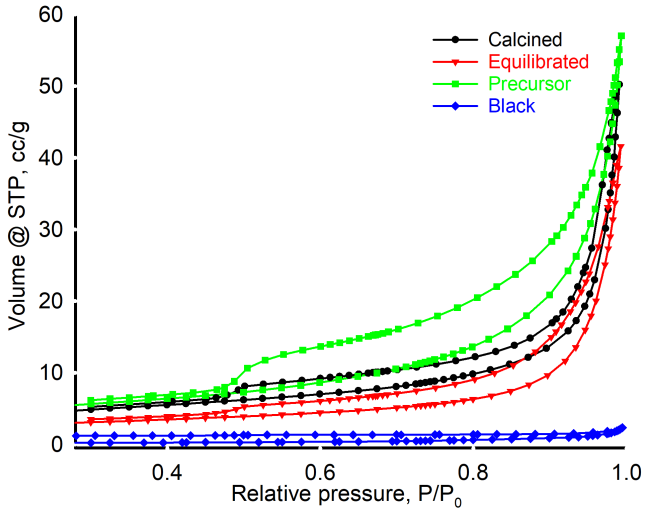

FIGURE 9 N_2 adsorption-desorption isotherms of VPP calcined, equilibrated-catalyst and VPO precursor

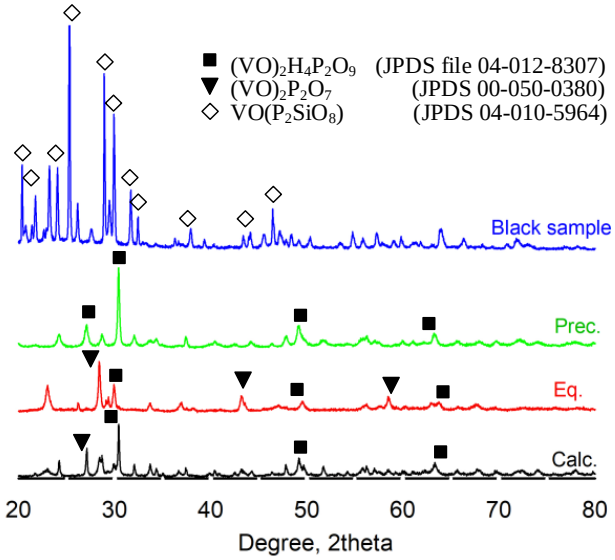

FIGURE 11 XRD pattern of VPP calcined, equilibrated-catalyst, VPO precursor and the black sample.

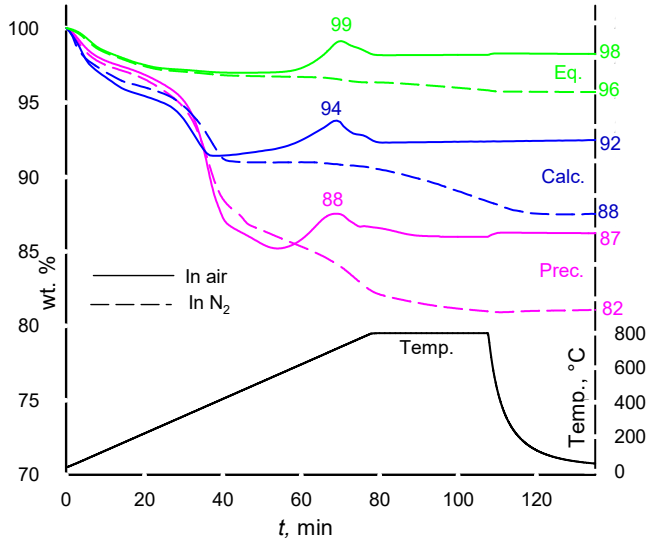

FIGURE 10 TGA analysis for VPP precursor, calcined, and equilibrated catalyst in air and nitrogen

only has physisorbed water to lose. Calcined VPP and precursor have around 5 % and 15 % of chemisorbed water in their structure. At 300 °C, the rate of mass loss increases due to the volatilization of other chemical compounds.

XRD detected a single phase of $VO(HPO_4) \cdot 0.5\,H_2O$ in the VPO precursor (JPDS file 04-012-8307). The main diffraction peaks are at 27.0°, 30.5°, 49.0°, and 63.3°, which are associated with vanadyl hydrogen phosphate hydrate (Figure 11).

The VPP calcined comprises two main phases of $VO(HPO_4) \cdot 0.5\,H_2O$ ($(VO)_2H_4P_2O_9$) and $(VO)_2P_2O_7$. XRD for calcined and precursor are similar, however, the peaks associated with the $(VO)_2P_2O_7$ phase are sharper, which indicates a higher degree of crystallinity (this is expected after calcination). In addition, it has a new peak at 23°, assigned to the $(VO)_2P_2O_7$ active phase (JPDS file 00-050-0380) (the rest of peaks of this phase, at 28° and 30°, overlap with those of $(VO)_2H_4P_2O_9$). The peaks at 24.0°, 27.0°, 28.8°, and 30.5°, are associated with vanadyl hydrogen phosphate hydrate and vanadyl hydrogen phosphate. The peak at 63.2° is associated only with the vanadyl hydrogen phosphate phase.

The equilibrated-catalyst sample contains mainly $(VO)_2P_2O_7$, as the peaks associated with this phase are more intense than the peaks of the other phases (peaks at 23.0°, 28.5°, 30.0°, 43.0°, and 58.8°). The $VO(HPO_4) \cdot 0.5\,H_2O$ ($(VO)_2H_4P_2O_9$) is absent of this sample. These data indicate that the $(VO)_2P_2O_7$ phase forms under reaction conditions at the expense of the $(VO)_2H_4P_2O_9$ phase. This is also in line with the water loss detected by TGA (Figure10).

The shape of the black particles diffractogram is completely different and contains $VO(P_2SiO_8)$ (JPDS file 04-010-5964) indicative that the shell of silica has interacted with the VPO phases. The peaks associated with the $VO(P_2SiO_8)$ phase are more intense compared to the peaks of other phases. The sample contains smaller amounts of other phases that might be $(VO)_2P_2O_7$, VOP_2O_6 and/or SiO_2 which is coherent with the SEM-EDS. The main diffraction peaks for the black samples are at 20.5°, 23.8°, and 29.0°, which are associated with vanadyl phosphate silicate. The peak at 25.2° is due to silicon oxide.

Figure 12 and 13 represent the XPS spectra of the equilibrated and calcined catalyst. The peak near 522 eV corresponds to lattice oxygen. $V2p_{3/2}$ binding energies are listed in Table 3. The $V2p_{3/2}$ peak corresponds to the contribution of different vanadium oxidation states, typically V^{5+} (517.0 eV to 516.9 eV and V^{4+} (516.3 eV to 516.1 eV)[59,60]. A contribution at 515.4 eV has been assigned to V^{3+} [61,62]. The $V2p_{3/2}$ signal centered around 516 eV (516.3 eV to 516.1 eV) indicates that most of V species are at an V^{4+} oxidation state. In samples with a lower particle size, the maximum shifts to lower binding energy, which corresponds to a lower degree of oxidation (amount of oxidized species as V^{5+}) is lower in this case.

TABLE 3 $V2p_{3/2}$ binding energies (eV)

No.	Sample	$V2p_{3/2}$ (eV)
1	Eq. 90 µm< d_p <120 µm	515.8
2	Eq. 45 µm< d_p <90 µm	515.4
3	Eq. d_p <45 µm	516.5
4	Eq. after 24 h in steam	516.5
5	Calc. after 789 °C in air	516.5
6	Calc. d_p >120 µm	516.4
7	Calc. 90 µm< d_p <120 µm	516.5
8	Calc. 45 µm< d_p <90 µm	515.8
9	Calc. d_p <45 µm	515.6

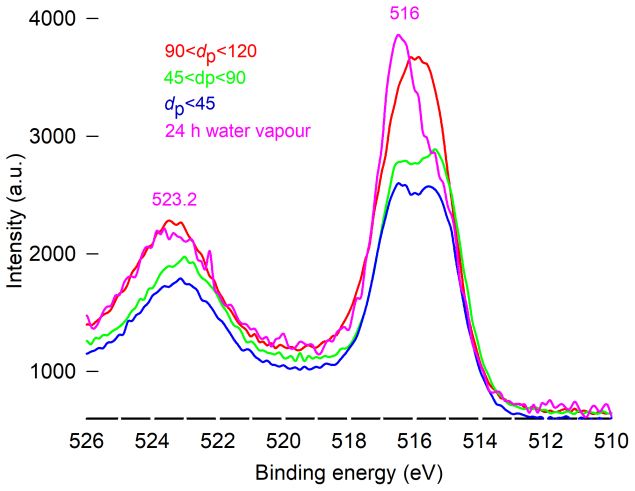

FIGURE 12 XPS spectrum of equilibrated-catalyst of < d_p45 µm, 45 µm< d_p <90 µm, 90 µm< d_p <120 µm, and after 24 h in steam from 530 eV to 510 eV

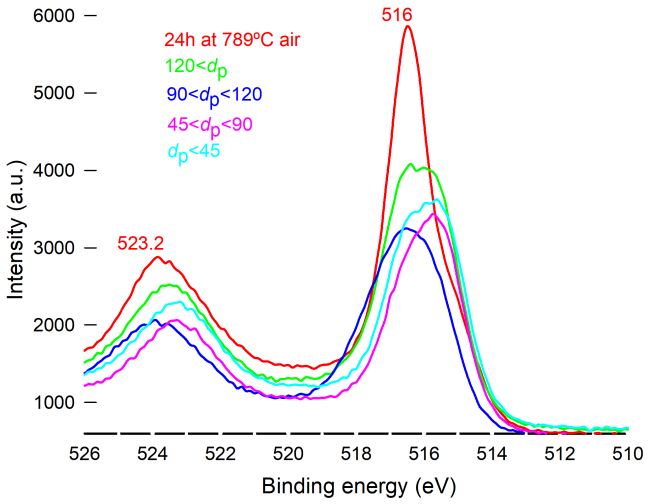

FIGURE 13 XPS spectrum of calcined-catalyst of after 789 °C in air, < d_p45 µm, 45 µm< d_p <90 µm, 90 µm< d_p <120 µm and 120 µm< d_p from 530 eV to 510 eV

Based on the XRD analyses of the four samples, almost all of the $(VO)_2H_4P_2O_9$ ($VO(HPO_4)\cdot 0.5\,H_2O$) phase in VPP catalyst transforms to $(VO)_2P_2O_7$ phase during the partial oxidation of n-butane to maleic anhydride. Before and after the reaction (both in calcined and equilibrated VPP), $(VO)_2P_2O_7$ was the main phase.

VPP precuror, calcined catalyst and equilibrated catalyst present signals that corresponds to a mixture of V-P-O phases ($(VO)_2P_2O_7$ and $VOPO_4$) (Figure 11, 16, 15). Chemical bonds in these phases are similar and undifferentiable. Calcined catalyst has a mixture of different VPO phases. Raman detects smaller crystals that are invisible by XRD (Figure 15 and 16). Note that we did not include the spectra for the precursor due to fluorescence problems.

The equilibrated-catalyst is more homogeneous and mainly consists of $(VO)_2P_2O_7$ (inferred from both Raman and XRD). The crystal phases of the equilibrated-catalyst are invariant with the temperature up to 300 °C under oxidation conditions. So, any change in the crystal structure or chemical bonds occurs at higher temperatures. In the equilibrated-catalyst, SiO_2 interacted with VPO and formed a V-Si-P-O mixed phase(Figure 15). According to Raman some VPO bonds are detected at ambient temperature, could be $\alpha-VOPO_4$. However, at higher temperature the bands related to $(VO)_2P_2O_7$ and V_2O_5 are small (peak at 140) due to the desgregation of VPO phases. In the black sample, V-P-O-Si phases and some incipient V_2O_5 formed that indicates that VPO phases are desagregating (Figure 15).

The Raman spectra of the black samples has a broad band from 900 cm^{-1} to 1000 cm^{-1} at room temperature,

that becomes sharper at higher temperature. At 300 °C, new peaks appear near 930 cm^{-1} to 1100 cm^{-1} that belongs to VPO phases, along with broad signals between 850 cm^{-1} to 950 cm^{-1} and two more broad peaks between 500 cm^{-1} to 550 cm^{-1}. In line with the XRD (Figure 11), Raman indicates a mixture of structures in the black particles that interconvert between them. In addition, a small feature that appear near 140 cm^{-1} at room temperature becomes more intense and sharper when at higher temperature (100 °C to 300 °C). This peak, along with another peak near 990 cm^{-1} (that overlaps with the signal form VPO phases) are the most intense Raman bands of V_2O_5 [57]. The presence of V_2O_5 indicates some disaggregation of VPO phases in the black particles.

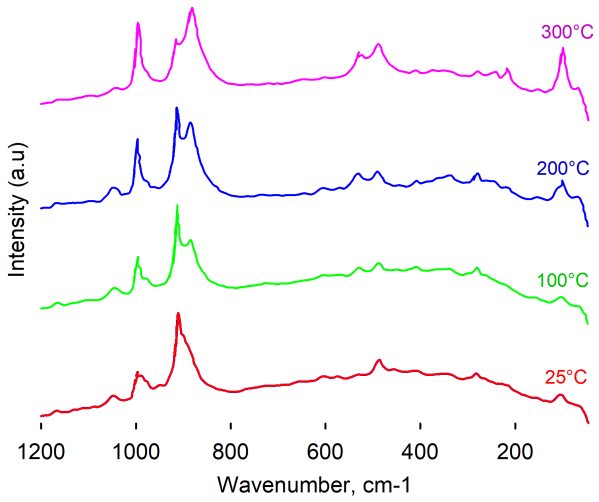

FIGURE 14 Raman spectroscopy characterization of black samples

The deactivation mechanisms during the oxidation of n-butane to maleic anhydride comprises the crystallization of amorphous phase(s) on the surface, coking and accumulation of carbonaceous species, the over-reduction of V^{4+} to V^{3+} sites or over-oxidation of V^{4+} to V^{5+} sites, loss of phosphorus, agglomeration, and sintering of the catalyst surface [58].

3.2.1 | Effect of particle size

In all samples, XRD diffractograms indicate that $(VO)_2P_2O_7$ is present. $(VO)_2P_2O_7$ phase forms large crystals and aggregates. Raman identifies other phases that are invisible to XRD because the crystals are too small to give a diffraction pattern.

Raman spectra of calcined catalyst have two bands near 930 cm^{-1} to 980 cm^{-1}, along with smaller signals in the region of 1000 cm^{-1} to 1025 cm^{-1} that correspond to P-O-P, V-O-P and P-O bonds [63]. These bonds indicate the presence of a mixture of α-$VOPO_4$, $VOPO_4$ hydrated and $VO(HPO_4)$ hydrated phases (Figure16) [64]. Raman spectroscopy characterization of calcined VPP after 789 °C in air has some heterogeneity, with the two sharp peaks near 140 cm^{-1} and 990 cm^{-1} in most of the points, which indicates V_2O_5 (Figure16(c)).

The equilibrated catalyst at room temperature has a sharp band near 930 cm^{-1}, characteristic of the $(VO)_2P_2O_7$ phase, in line with XRD data (Figure15). Raman spectra of equilibrated VPP heated up to 300 °C in air and then cooled down to room temperature did not really change (Figure 15), confirming the $(VO)_2P_2O_7$ phase is stable. The calcined catalyst, on the other-hand, undergoes a irreversible phase change when heated in the presence of oxygen. The peak intensity of the Raman spectra of calcined VPP heated up to 100 °C to 300 °C in air decreased significantly, and it remained low even after cooling down to room temperature (Figure 16).

Equilibrated VPP 90 µm< d_p <120 µm has a certain degree of heterogeneity, it is mainly $(VO)_2P_2O_7$ (Raman band near 930 cm^{-1}),in accordance with XRD, but also other VPO phases (Figure 15,(b)) like α_{II}-$VOPO_4$ and γ-$VOPO_4$. These other phases are minor, since only Raman detected them in some points and XRD did not detect any. Raman recorded similar phases for d_p<45 µm (Figure 15(a)) and 24 h in steam samples (Figure 15(c)). Sample 45 µm< d_p <90 µm has less heterogeneity (both XRD and Raman detected only $(VO)_2P_2O_7$). Raman spectra of equilibrated VPP of d_p <45 µm has peaks of $(VO)_2P_2O_7$, in line by XRD (Figure 15(a)). Raman also detected some points characteristic of β-$VOPO_4$. Raman spectra of equilibrated VPP after 24 h in steam, also has a band near 930 cm^{-1} (belonging to $(VO)_2P_2O_7$) in most of the points, and some small spots of a mixture of other VPO phases, such as α_{II}-$VOPO_4$ and γ-$VOPO_4$ (Figure 15(c)).

4 | CONCLUSIONS

In this study, we examined the morphological changes of VPP due to temperature excursions. After several years at commercial operating conditions, the VPP particle size dropped to 59 µm from the original 67 µm due to attrition [65]. The surface of the equilibrated-catalyst is smoother and shinier than that of the fresh catalyst and most asperities were cleaved. The catalytic surface area of the fresh catalyst decreased from 23 $m^2\ g^{-1}$ to 12 $m^2\ g^{-1}$ in the equilibrated-catalyst which was due to sintering: a) crystallite growth of the catalytic phase and/or b) pore collapse on crystallites of the active phase. The fresh catalyst has a higher pore volume (0.14 $cm^3\ g^{-1}$) compared to the equilibrated catalyst (0.09 $cm^3\ g^{-1}$), and the particle density of the catalyst increase slightly from 1713 $kg\ m^{-3}$

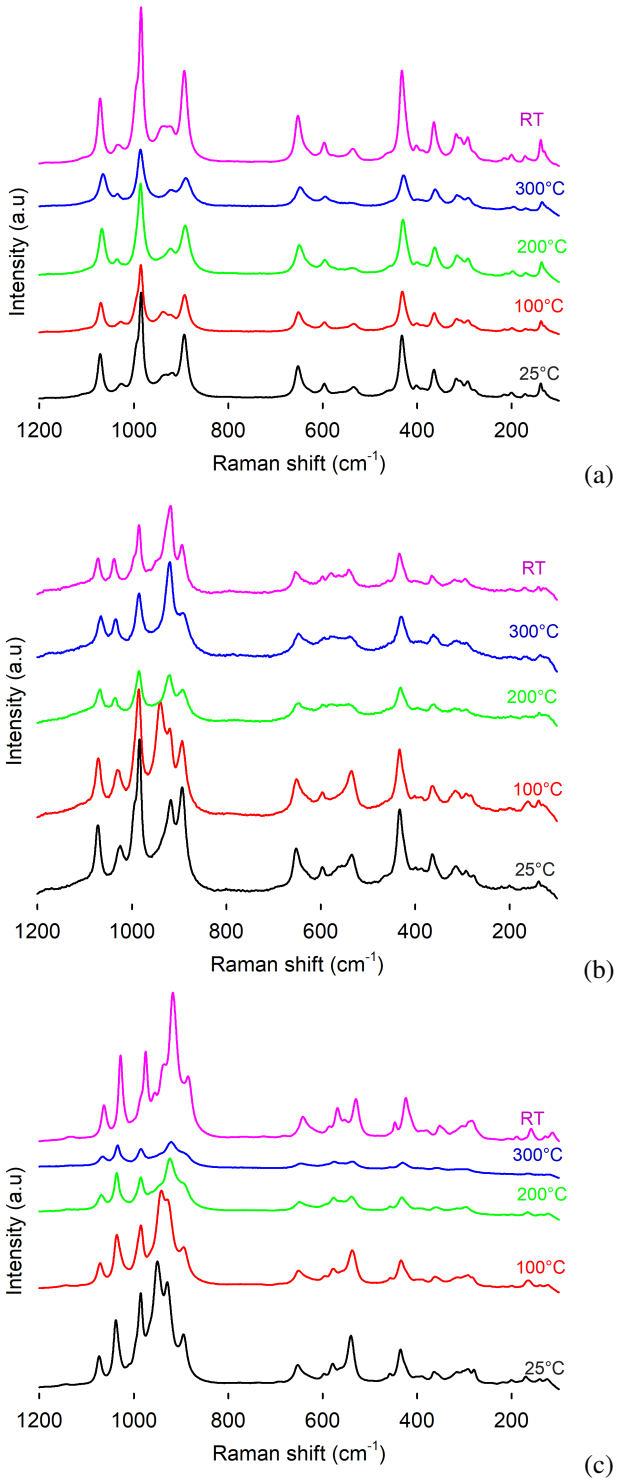

FIGURE 15 Raman spectroscopy characterization of equilibrated VPP a) d_p <45 μm, b) 90 μm< d_p <120 μm, and c) after 24 h in steam.

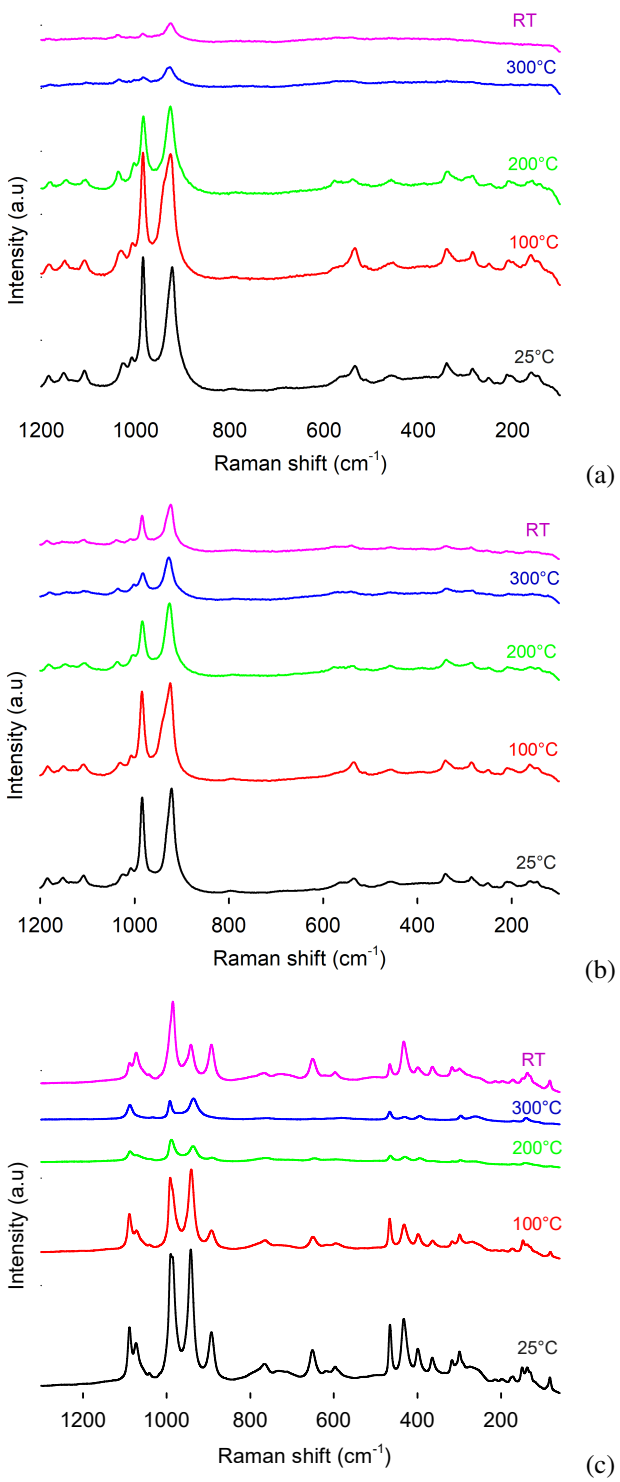

FIGURE 16 Raman spectroscopy characterization of calcined VPP a) d_p <45 μm, b) d_p >120 μm, and c) after 789 °C in air.

to 1959 kg m^{-3} due to loss of porosity. Either the pores collapse or they become fouled by reactants, intermediates, and/or products [66]. Metal and metal oxidess sinter moderately fast in oxygen (the VPP catalyst turned black above 710 −720 °C in the air) [65]. The silica shell in the calcined catalyst reacts with the active phase ($(VO)_2P_2O_7$) and forms $VO(P_2SiO_8)$ above 700 °C (black sample). Since VPP sinters above> 650 °C [65],

the reactor temperature must have increased beyond its operating temperature of 400 °C. In fact, the local temperature at the sparger tips would have to have risen above 700 °C to turn the catalyst black. Small particles ($d_p < 45$ µm) turned black more readily than larger particles, which may be due to their lower mass and higher surface-to-volume ratio.

References

[1] Clarivate Analytics, Web of Science™ Core Collection **2021**, accessed on 29 April 2021, http://apps.webofknowledge.com.

[2] M. R. Thompson, C. Tzoganakis, G. L. Rempel, *Polym. Eng. Sci*. **1998**, *38*, 1694.

[3] P. Wongthong, C. Nakason, Q. M. Pan, G. L. Rempel, S. Kiatkamjornwong, *Eur. Polym. J*. **2014**, *59*, 144.

[4] P. Wongthong, C. Nakason, Q. M. Pan, G. L. Rempel, S. Kiatkamjornwong, *Eur. Polym. J*. **2013**, *49*, 4034.

[5] N. J. van Eck, L. Waltman, *Sci*. **2010**, *84*, 523.

[6] M. Witko, R. Tokarz, J. Haber, K. Hermann, *J. Mol. Catal. A: Chem*. **2001**, *166*, 59.

[7] Z.-Y. Xue, G. L. Schrader, *J. Phys. Chem. B* **1999**, *103*, 9459.

[8] J. K. Bartley, N. F. Dummer, G. J. Hutchings, *Met. Oxide Catal*. **2008**, 499.

[9] V. Guliants, J. B. Benziger, S. Sundaresan, N. Yao, I. Wachs, *Catal. Lett*. **1995**, *32*, 379.

[10] G. Mestl, D. Lesser, T. Turek, *Top. Catal*. **2016**, *59*, 1533.

[11] M. Heenemann, C. Heine, M. Hävecker, A. Trunschke, R. Schlögl, *J. Phys. Chem. B* **2018**, *122*, 695.

[12] E. Bordes, *Catal. Today* **1988**, *3*, 163.

[13] E. Bordes, *Catal. Today* **1987**, *1*, 499.

[14] G. S. Patience, R. E. Bockrath, J. D. Sullivan, H. S. Horowitz, *Ind. & Eng. Chem. Res*. **2007**, *46*, 4374.

[15] J. W. Johnson, D. C. Johnston, A. J. Jacobson, J. F. Brody, *J. Am. Chem. Soc*. **1984**, *106*, 8123.

[16] Y. E. Gorbunova, S. Linde, Doklady Akademii Nauk, volume 245, Russian Academy of Sciences **1979**, pp. 584–588.

[17] B. He, L. Nan, Z. Li, B. Wen, J. Niu, R. Liu, *Chem*. **2019**, *4*, 662.

[18] N. Ballarini, F. Cavani, C. Cortelli, M. Ricotta, F. Rodeghiero, F. Trifiro, C. Fumagalli, G. Mazzoni, *Catal. Today* **2006**, *117*, 174.

[19] F. Cavani, F. Trifiro, *Appl. Catal. A: Gen*. **1997**, *157*, 195.

[20] M. Ai, *J. Catal*. **1986**, *101*, 389.

[21] G. Centi, D. Pesheva, F. Trifiro, *Appl. Catal*. **1987**, *33*, 343.

[22] G. Centi, F. Trifiro, *Chem. Eng. Sci*. **1990**, *45*, 2589.

[23] E. Bordes, *Catal. Today* **1993**, *16*, 27.

[24] G. Centi, T. Tosarelli, F. Trifiro, *J. Catal*. **1993**, *142*, 70.

[25] F. Wang, J.-L. Dubois, W. Ueda, *Appl. Catal. A: Gen*. **2010**, *376*, 25.

[26] A. Martin, C. Janke, V. N. Kalevaru, *Appl. Catal. A: Gen*. **2010**, *376*, 13.

[27] G. Centi, F. Trifirpò, *J. Mol. Catal*. **1986**, *35*, 255.

[28] G. Centi, *Catal. Today* **1993**, *16*, 5.

[29] A. Shekari, G. S. Patience, R. E. Bockrath, *Appl. Catal. A: Gen*. **2010**, *376*, 83.

[30] G. S. Patience, R. E. Bockrath, *Appl. Catal. A: Gen*. **2010**, *376*, 4.

[31] K. W. Hutchenson, C. La Marca, G. S. Patience, J.-P. Laviolette, R. E. Bockrath, *Appl. Catal. A: Gen*. **2010**, *376*, 91.

[32] A. Shekari, G. S. Patience, R. E. Bockrath, *Appl. Catal. A: Gen*. **2010**, *376*, 83.

[33] R. M. Contractor, *Chem. Eng. Sci*. **1999**, *54*, 5627.

[34] G. S. Patience, Experimental Methods and Instrumentation for Chemical Engineers, Elsevier, Amsterdam **2017**.

[35] G. Centi, G. Golinelli, F. Trifiro, *Appl. Catal*. **1989**, *48*, 13.

[36] L. M. Cornaglia, E. A. Lombardo, Studies in Surface Science and Catalysis, volume 90, Elsevier **1994**, pp. 429–440.

[37] G. Busca, G. Centi, F. Trifiro, V. Lorenzelli, *J. Phys. Chem*. **1986**, *90*, 1337.

[38] M. Abon, J.-C. Volta, *Appl. Catal. A: Gen*. **1997**, *157*, 173.

[39] G. Centi, F. Trifiro, J. R. Ebner, V. M. Franchetti, *Chem. Rev*. **1988**, *88*, 55.

[40] J. Ebner, M. Thompson, *Catal. Today* **1993**, *16*, 51.

[41] L. Cornaglia, E. Lombardo, J. Andersen, J. G. Fierro, *Appl. Catal. A: Gen*. **1993**, *100*, 37.

[42] A. M. Wernbacher, M. Eichelbaum, T. Risse, S. Cap, A. Trunschke, R. Schlögl, *J. Phys. Chem. C* **2018**, *123*, 8005.

[43] W. R. Moser, Advanced catalysts and nanostructured Materials: modern synthetic methods, Academic press **1996**.

[44] G. S. Patience, E. Bordes-Richard, *Appl. Catal. A: Gen*. **2010**, *376*, 1.

[45] G. J. Hutchings, C. J. Kiely, M. T. Sananes-Schulz, A. Burrows, J. C. Volta, *Catal. Today* **1998**, *40*, 273.

[46] P. Amorós, R. Ibáñez, E. Martínez-Tamayo, A. Beltrán-Porter, D. Beltrán-Porter, G. Villeneuve, *Mater. Res. Bull*. **1989**, *24*, 1347.

[47] H. Li, M. Rostamizadeh, K. Mameri, D. C. Boffito, N. Saadatkhah, M. G. Rigamonti, G. S. Patience, *Can. J. Chem. Eng*. **2019**, *97*, 2242.

[48] M. G. Rigamonti, Y.-X. Song, H. Li, N. Saadatkhah, P. Sauriol, G. S. Patience, *Can. J. Chem. Eng*. **2019**, *97*, 2251.

[49] N. Saadatkhah, S. Aghamiri, M. R. Talaie, G. S. Patience, *Can. J. Chem. Eng*. **2019**, *97*, 2299.

[50] N. Saadatkhah, A. Carillo Garcia, S. Ackermann, P. Leclerc, M. Latifi, S. Samih, G. S. Patience, J. Chaouki, *Can. J. Chem. Eng*. **2020**, *98*, 34.

[51] M. O. Guerrero-Pérez, G. S. Patience, M. A. Bañares, *Can. J. Chem. Eng*. **2021**, *99*, 97.

[52] M. J. D. Mahboub, J. Wright, D. C. Boffito, J.-L. Dubois, G. S. Patience, *Appl. Catal. A: Gen*. **2018**, *554*, 105.

[53] N. F. Dummer, W. Weng, C. Kiely, A. F. Carley, J. K. Bartley, C. J. Kiely, G. J. Hutchings, *Appl. Catal. A: Gen*. **2010**, *376*, 47.

[54] M. J. Darabi Mahboub, S. M. Jazayeri, O. Chub, J.-L. Dubois, G. S. Patience, *Can. J. Chem. Eng*. **2021**, *99*, 1475.

[55] R. Bardestani, G. S. Patience, S. Kaliaguine, *Can. J. Chem. Eng*. **2019**, *97*, 2781.

[56] J. Do, R. P. Bontchev, A. J. Jacobson, *Chem. Mater*. **2001**, *13*, 2601.

[57] M. Guerrero-Pérez, J. G. Fierro, M. Vicente, M. Banares, *J. Catal*. **2002**, *206*, 339.

[58] R. M. Blanco, A. Shekari, S. G. Carrazán, E. Bordes-Richard, G. S. Patience, P. Ruiz, *Catal. Today* **2013**, *203*, 48.

[59] R. López-Medina, J. Fierro, M. O. Guerrero-Pérez, M. Bañares, *Appl. Catal. A: Gen*. **2011**, *406*, 34.

[60] F. Richter, H. Papp, G. U. Wolf, T. Götze, B. Kubias, *Fresenius' J. Anal. Chem*. **1999**, *365*, 150.

[61] M. Ziolek, I. Nowak, *Catal. today* **2003**, *78*, 543.

[62] J. F. Moulder, W. F. Stickle, P. E. Sobol, K. D. Bomben, Handbook of X-ray photoelectron spectroscopy, Eden Praire, Minn **1992**.

[63] M. A. Carreon, V. V. Guliants, M. O. Guerrero-Pérez, M. A. Bañares, *Microporous mesoporous materials* **2004**, *71*, 57.

[64] F. B. Abdelouahab, R. Olier, N. Guilhaume, F. Lefebvre, J. Volta, *J. Catal*. **1992**, *134*, 151.

[65] C. H. Bartholomew, *Appl. Catal. A: Gen*. **2001**, *212*, 17.

[66] M. D. Argyle, C. H. Bartholomew, *Catal*. **2015**, *5*, 145.

□